Journal Homepage: https://dergipark.org.tr/tr/pub/isibted

Isı Bilimi ve Tekniği Dergisi

Archive: https://tibtd.org.tr/dergi

A Characterization of Cement Paste Degradation Exposed to Elevated Temperatures Conditions Using TG-DTG/DSC, XRD, SEM, and FTIR Analyses

Duygu ADIGÜZEL[1], Jale NAKTİYOK[1]*, Ahmet Ferhat BİNGÖL[2]

[1] *Engineering Faculty, Department of Chemical Engineering, Atatürk University, 25240, Erzurum, Turkey*
[2] *Engineering Faculty, Department of Civil Engineering, Atatürk University, 25240, Erzurum, Turkey*

A R T I C L E I N F O

2026, vol. 46, no.1, pp. 130-140

doi: 10.47480/isibted.1800582

Research Article
Received: 10 October 2025
Accepted: 18 February 2026

* *Corresponding Author*
e-mail: jalenaktiyok@atauni.edu.tr

Keywords:
Cement paste
High temperature
TG-DTG/DSC
Structural analysis
Kinetics analysis

ORCID Numbers in author order:
0000-0002-8854-5501
0000-0002-6316-4112
0000-0002-8798-8343

A B S T R A C T

The high-temperature behavior of CEM I cement paste was investigated using TG–DTG/DSC, BET, XRD, SEM, and FTIR analyses to evaluate the structural and chemical modifications occurring between 25 and 1000°C under air atmosphere. The degradation profiles from TG–DTG/DSC experiments revealed three distinct regions: (i) dehydration of the C–S–H gel and pore water, (ii) dehydroxylation of portlandite, and (iii) decarbonation of calcite. Characteristic temperatures for each degradation step were determined, and kinetic parameters were calculated using the Ortega method. Accordingly, the activation energy of Region 1 was determined to be 42.92 kJ/mol. For Region 2, the activation energy was calculated as 151.82 kJ/mol, while in Region 3 it was found to be 152.11 kJ/mol. BET analysis indicated extensive cracking of the micropore structure, while XRD, SEM, FTIR analysis provided insights into phase transformations and microstructural evolution in pastes exposed to elevated temperatures. Also, the effect of heating rate on the thermal degradation of the cement paste was investigated by using DSC data. It was observed that as the heating rate increased, the degradations shifted towards higher temperatures. These findings contribute to a better understanding of the thermal stability and degradation mechanisms of cementitious materials under fire conditions.

Yüksek Sıcaklık Koşullarına Maruz Kalan Çimento Hamurunun Bozunmasının TG-DTG/DSC, XRD, SEM ve FTIR Analizleri ile Karakterizasyonu

M A K A L E B İ L G İ S İ

Anahtar Kelimeler:
Çimentu hamuru
Yüksek sıcaklık
TG-DTG/DSC
Yapısal analizler
Kinetik analiz

Ö Z E T

CEM I çimento hamurunun yüksek sıcaklık davranışı, hava atmosferinde 25 ile 1000°C arasında meydana gelen yapısal ve kimyasal değişiklikleri değerlendirmek için TG–DTG/DSC, BET, XRD, SEM ve FTIR analizleri kullanılarak incelenmiştir. TG–DTG/DSC deneylerinden elde edilen bozunma profilleri üç farklı bölgeyi ortaya çıkarmıştır: (i) C–S–H jelinin ve gözenek suyunun dehidrasyonu, (ii) portlanditin dehidroksilasyonu ve (iii) kalsitin dekarbonizasyonu. Her bozunma aşaması için karakteristik sıcaklıklar belirlenmiş ve Ortega yöntemi kullanılarak kinetik parametreler hesaplanmıştır. Buna göre, 1. bölgeye ait aktivasyon enerjisi 42.92 kJ/mol olarak belirlenmiştir. 2. bölge için aktivasyon enerjisi 151.82 kJ/mol olarak hesaplanmış olup, 3. bölgede ise 152.11 kJ/mol olarak bulunmuştur. BET analizi, mikro gözenek yapısında yaygın çatlama olduğunu gösterirken, XRD, SEM ve FTIR analizleri ise yüksek sıcaklıklara maruz kalan çimento hamurlarındaki faz dönüşümleri ve mikroyapısal dönüşüm hakkında bilgiler sağlamıştır. Ayrıca ısıtma hızının, çimento hamurunun termal bozunması üzerindeki etkisi DSC verilerinden yararlanılarak araştırılmıştır. Isıtma hızı arttıkça bozunmaların daha yüksek sıcaklıklara doğru kaydığı gözlenmiştir. Bu bulgular, yangın koşullarında çimento esaslı malzemelerin termal stabilitesi ve bozulma mekanizmalarının daha iyi anlaşılmasına katkıda bulunmaktadır.

NOMENCLATURE

TG	Thermal Gravimetry	CH	Portlandite $(CaOH)_2$
DTG	Differantial Thermal Gravimetry	α	Conversion degree
DSC	Differantial Scanning Calorimetry	β	Heating rate (°C/min)
FTIR	Fourier Transform Infrared Spectroscopy	Ea	Activation energy (kJ/mol)
BET	Brunauer–Emmett–Teller Analysis	T	Temperature (K)
XRD	X-Ray Diffraction	g(α)	Reaction mechanism
SEM	Scanning Electron Microscopy	R	Ideal gas constant (J/mol.K)
C-S-H	Calcium silicate hydrate	A	Pre-exponential factor

INTRODUCTION

High temperatures lead to significant deterioration in concrete as various physical and chemical reactions gradually break down the cement gel structure. As a result, concrete experiences losses in strength and durability, increased shrinkage by drying, the development of structural cracks, and noticeable color changes in damaged areas (Handoo et al. 2002; Poon et al. 2003). Most of this damage occurs within the cement paste, which serves as the primary binding phase of concrete (Bingöl&Gül 2009; Tantawy 2017). Heat-induced chemical reactions and decomposition within the cement paste critically influence the mechanical behavior of concrete. In particular, dehydration and the evaporation of capillary water generate elevated internal pore pressures, which can even trigger explosive.

To better understand these deteriorations, it is crucial to examine the microstructural and phase transformations within the cement paste. The primary hydration products—C–S–H (calcium silicate hydrate) gel and C–H (calcium hydroxide)—are largely responsible for the mechanical integrity of the material. As temperature increases, dehydration begins with the loss of free water and progresses with the release of bound water from the C–S–H gel. Due to its amorphous structure, reported temperature ranges for C–S–H dehydration vary considerably (100–250°C, 180–300°C, and even 150–1000°C). This dehydration causes internal stresses and micro cracking, while the dehydroxylation of C–H at 450–550°C further contributes to damage (Tantawy 2017; Arıöz 2007). At temperatures above 600–800°C, the cement paste loses the majority of its strength (Khoury 1992).

The behavior of concrete at elevated temperatures is influenced by both internal and external factors. Internal factors include the type of aggregate and cement, mix composition, and moisture content, while external factors involve the heating rate, the maximum temperature reached, the duration at that temperature, and the cooling conditions (Poon et al. 2001; Hüsem 2006). Although concrete generally exhibits some level of heat resistance, in certain applications it is necessary to produce mixes with enhanced fire resistance (Bingöl&Gül 2004). Evaluating the deterioration level of concrete exposed to elevated temperatures helps engineers determine whether a structure can be repaired or must be replaced (Poon et al. 2004).

In recent years, thermogravimetric analysis (TGA) has become a key method for examining the high-temperature degradation of cementitious materials (Peng&Huang 2008). This technique provides deeper insight into the complex reactions and phase transitions that occur during heating. While many studies have investigated the effects of elevated temperatures on the mechanical properties of cement-based mixtures using one or more analytical methods, structural changes have often remained unaddressed.

In this study, the thermal behavior of cement paste was analyzed comprehensively using TG–DTG/DSC techniques, with particular focus on the effects of different heating rates. Kinetic parameters of the degradation processes were derived from TGA data to identify the controlling reaction mechanisms. Additionally, XRD, SEM, FTIR, and BET analyses were conducted to characterize the microstructural and phase transformations in cement paste exposed to high temperatures, offering a detailed assessment of its thermal stability. This study, by integrating thermal, structural, and microstructural findings, is expected to not only clarify the degradation mechanisms but also provide valuable insights for evaluating fire-induced damage and designing more fire-resistant cementitious materials.

EXPERIMENTAL STUDY

Materials and Methods

For the preparation of cement paste samples, CEM I 42.5 R cement was employed in this study. The paste was produced without aggregates, as the presence of aggregates could interfere with TG–DTG/DSC measurements. The water-to-cement ratio was fixed at 0.512. The mixtures were cast into stainless steel cubic samples of (50×50×50 mm) and cured under water for 28 days to ensure full hydration. After curing, the samples were oven-dried at 105°C for 24 hours.

The sample consists of hydrated cement paste prepared from Portland cement (CEM I 42.5 R cement) and water. Its chemical composition includes the primary cement clinker phases: C3S (alite), C2S (belite), C3A (tricalcium aluminate), C4AF (ferrite), and added calcium sulfate (gypsum). Following hydration, the paste contains typical reaction products such as calcium silicate hydrate (C–S–H), portlandite ($Ca(OH)_2$), ettringite, and physically adsorbed or capillary water.

The cement paste was subjected to elevated temperatures in a high-temperature furnace to observe its physical and chemical transformations. The samples were exposed to 200°C, 400°C, 600°C, and 800°C for 3 hours, while a non-heat-treated sample was kept as a reference. After heating, all specimens were cooled in air at ambient conditions.

A 300-ton ELE brand AUTOTEST 3000 hydraulic press was used to determine the compressive strength of raw and temperature-exposed samples. All samples were tested under a constant loading rate. According to TS EN 12390-3 (2010), this value should be between 0.2 MPa/s and 1.0 MPa/s. The concrete samples were crushed using a loading rate of 0.4 MPa/s. After thermal exposure at the designated temperatures, all specimens were cooled to room temperature before testing. Cubic samples were placed in the loading apparatus, and it was tested for each sample.

Thermogravimetric analysis (TG–DTG/DSC) was performed at NETZSCH STA 409 PC Luxx thermal analyzer, which provides high sensitivity to both temperature and weight changes. The balance and temperature control system can accurately record weight loss of 0.001 mg and temperature of 0.1 K. The calcined α-Al_2O_3 powder was used as the standard reference. Prior to the experiments, the instrument was calibrated using the standard calibration sets supplied by Netzsch. All thermal analyses were conducted under a gas flow rate of 90 mL/min. Approximately 20 mg of each sample was subjected to heating (25°C-1000°C) at atmospheric and non-isothermal conditions. The heating rates were 2.5, 5, and 10°C/min. From the TG–DTG/DSC curves, mass losses and characteristic temperatures—such as the onset (To), peak (Tp), and completion points (Tc) of dehydration, dehydroxylation, and decarbonization reactions—were determined to evaluate the thermal behavior of the cement paste.

The crystalline phases of the samples were identified by X-ray diffraction analysis (PANalytical Empyrean diffractometer). The measurements were performed at 25°C over a 2θ range of 20°–80° at rate of 2°/min.

Microstructural features were investigated through scanning electron microscopy (SEM) using a Zeiss Sigma 300 instrument. The functional groups present in the samples were analyzed by Fourier Transform Infrared (FT-IR) spectroscopy (Bruker VERTEX 70v spectrometer), collecting spectra in the 4000–400 cm^{-1} range.

Surface characteristics, including specific surface area, pore diameter, and pore size distribution, were evaluated using the Brunauer–Emmett–Teller (BET) and Barrett–Joyner–Halenda (BJH) methods. These analyses were carried out with a Micromeritics 3Flex surface analyzer. For BET analysis of cement paste, proper degassing is crucial to remove adsorbed moisture and volatile components without altering the hydrated phases. Typically, the degassing was performed under vacuum to prevent oxidation. The degassing temperature was generally kept low, around 70°C, to avoid decomposition of sensitive components like CH, while ensuring effective removal of surface-adsorbed species. The degassing duration was 24 hours, with a slow temperature ramp of 1°C/min, allowing gradual removal of moisture and minimizing structural damage. These conditions help ensure accurate measurement of the specific surface area and pore characteristics of the cement paste.

RESULTS AND DISCUSSION

Compressive Strength

Table 1 presents the compressive strengths of the cement paste samples exposed to 25°C, 200°C, 400°C, 600°C, and 800°C. The compressive strength of the samples subjected to 600°C and 800°C could not be measured due to extensive microstructural damage and loss of cohesion.

Table 1. Compressive strength of cement pastes at various temperatures.

Temperature (°C)	**25° C**	**200°C**	**400°C**	**600°C**	**800°C**
Compressive strenght (MPa)	50.4	34.1	33.5	-	-

The results demonstrate a clear decline in compressive strength with increasing temperature, which can be attributed to the dehydration of C–S–H gel, dehydroxylation of C–H, and the formation of micro cracks within the cement paste. This indicates that thermal exposure severely compromises the load-bearing capacity of the material.

Additionally, photographs of the samples in their pre-heating and post-heating conditions is presented in Figure 1. In Figure 1, the samples numbered 1, 2, 3, 4, and 5 correspond to specimens exposed to 25°C, 200°C, 400°C, 600°C, and 800°C, respectively. The photographs clearly show the macro-scale physical deterioration that occurs in cement mortar samples after exposure to high temperatures. The top row shows unheated samples with a dense and well-hydrated microstructure, featuring sharp edges, smooth surfaces, and no visible cracks. In contrast, the samples shown in the bottom row (after thermal treatment) exhibit clear signs of thermal damage. Visible features include surface cracks, edge spalling, localized material loss, and increased surface roughness. These changes are consistent with the expected microstructural degradation following dehydration of the C-S-H gel, decomposition of portlandite, and the resulting increase in internal pore pressure. The visual deterioration observed in the heated specimens therefore corroborates the decrease in mechanical performance measured after thermal exposure. As can be seen from the Figure 1, the mechanical strengths of the specimens heated to 600°C and 800°C could not be measured due to their severely degraded and fragmented condition.

Figure 1. The photographs of the samples in their pre-heating (a) and post-heating (b) conditions.

In the literature, it was reported that the mechanical strength of (without additives) cement paste decreases progressively with increasing temperature, demonstrating the inherent thermal vulnerability of unmodified CEM I systems when exposed to elevated temperatures (Abdelmelek&Lubloy 2021). In other study, it was reported that the compressive strength of cement paste decreases markedly with rising temperature (Boquera et al. 2021). The ordinary Portland cement (OPC) paste exhibited an initial strength of approximately 43 MPa, but after the first heating cycle at 200°C its strength dropped by about 40%. At both 200°C and 400°C, OPC paste showed a similar residual compressive strength of 28 ±5 MPa. However, upon heating to 800°C, a clear divergence in behavior was observed that OPC paste exhibited a dramatic reduction, dropping sharply to 6 ±1 MPa. These results indicate the significant loss of mechanical integrity in OPC paste at higher temperatures. The cement paste examined in our study also showed a continuous decrease in compressive strength with increasing temperature, with the most severe losses occurring beyond 400°C due to CH dehydroxylation and the collapse of the C–S–H structure. Notably, in our results the samples exposed to 600°C and 800°C became too damaged to test, which is consistent with the sharp mechanical deterioration reported by Boquera et al. (2021) for OPC paste at similar temperatures. These similarities confirm that unmodified Portland cement systems exhibit inherently poor thermal resistance, losing their mechanical integrity rapidly when exposed to elevated temperatures above 400–600°C.

XRD Analysis

The XRD patterns showing the phase composition of the cement paste samples are illustrated in Figure 2. The most prominent crystalline phases observed in the sample at 25°C are C–S–H, calcite, ettringite, and portlandite, which are typical hydration products. The intensity of the portlandite peaks decreases significantly at 400°C and completely disappears at 600°C. Moreover, noticeable peaks corresponding to belite (C2S) and alite (C3S) appear at 400°C and become more pronounced at 600°C and 800°C. This indicates that a substantial portion of C–S–H undergoes decomposition starting at around 400°C, and this process continues with increasing temperature. It has also been reported in the literature that distinguishing between C2S and C3S peaks is challenging due to their overlapping diffraction characteristics (Tantawy 2017; Poon et al. 2004; Peng&Huang 2008).

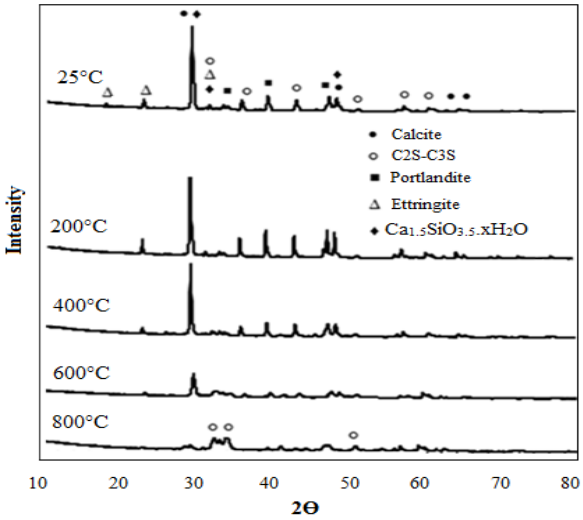

Figure 2. XRD result of cement paste at different temperatures.

SEM-EDS Analysis

The SEM images of cement paste samples exposed to a temperature range of 25–800°C are shown in Figure 3. The images illustrate the progressive changes in the microstructure and phase composition caused by dehydration and decomposition processes.

At 25°C, the microstructure exhibits a heterogeneous morphology characterized by C–S–H gel, CH (portlandite) crystals, and needle-like ettringite formations, which are typical hydration products of cement paste. Minor micro cracks are also visible.

At 200°C, the general morphology remains relatively intact; however, early signs of C–S–H degradation can be observed, indicating the beginning of the dehydration process.

At 400°C, the microstructure reveals partially dehydrated cement particles along with remnants of hexagonal portlandite plates, suggesting significant phase transformation.

At 600°C, the morphology changes more distinctly, showing the presence of well-formed cubic calcite crystals and a more porous structure, reflecting the extensive decomposition of hydrated products.
calcite crystals and a more porous structure, reflecting the extensive decomposition of hydrated products.

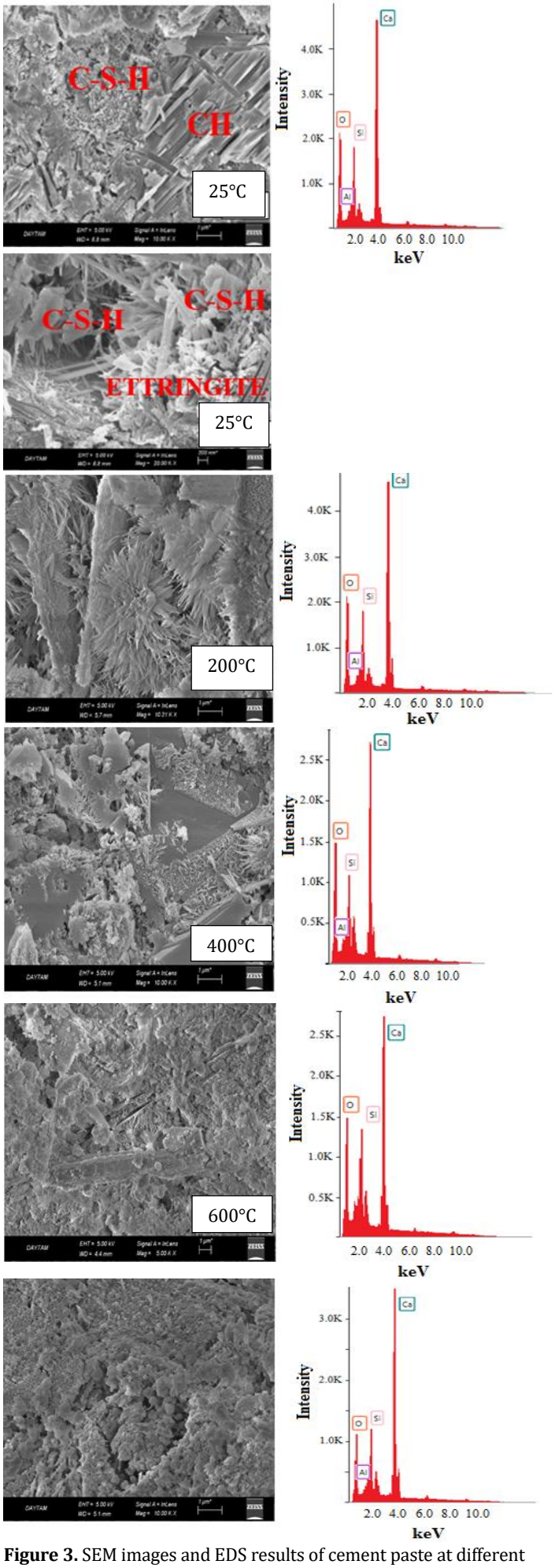

Figure 3. SEM images and EDS results of cement paste at different temperatures.

Finally, at 800°C, the SEM image displays a severely damaged and porous matrix dominated by dehydration products, particularly CaO, confirming the collapse of the cementitious gel and the loss of structural integrity.

The EDS analyses of cement pastes heated at 25, 200, 400, 600 and 800°C reveal a progressive surface chemical evolution with increasing temperature, consistent with previous observations in carbonated cement systems (Li et al. 2022). At 200°C, the surface composition is dominated by contributions from hydrated phases, with relatively balanced Si and Ca signals indicative of intact C–S–H and CH. By 400°C, partial dehydration of C–S–H and initial decomposition of portlandite lead to a modest increase in the relative Ca signal. At 600°C and particularly at 800°C, EDS spectra show pronounced Ca enrichment at the sample surface, while Si and Al signals diminish in relative intensity; this behavior is attributed to CH decomposition to CaO and surface segregation or recrystallization of Ca-rich phases, and it matches the microstructural changes reported in the literature (Li et al. 2022). In the study, the influence of cement paste hydration at different W/C ratios on its microstructure was investigated, and SEM-EDS analysis was performed (Kasaniya et al. 2025). The authors noted that the presence of abundant Ca deposits, particularly on the surface, could lead to inaccurate readings of other elemental peaks.

FT-IR Analysis

The FT-IR profiles of the cement paste samples subjected to varying temperatures are presented in Figure 4. The spectra display characteristic absorption bands corresponding to the main functional groups and phases of hydrated and dehydrated cement paste. The –OH stretching vibrations associated with structural and adsorbed water appear in the ranges of 3500–3400 cm^{-1} and 1650–1600 cm^{-1}. The carbonate (CO_3^{-2}) vibrations are observed around 1420 cm^{-}400 cm^{-1}, 870–850 cm^{-1}, and 700–600 cm^{-1}, confirming the presence of calcite.

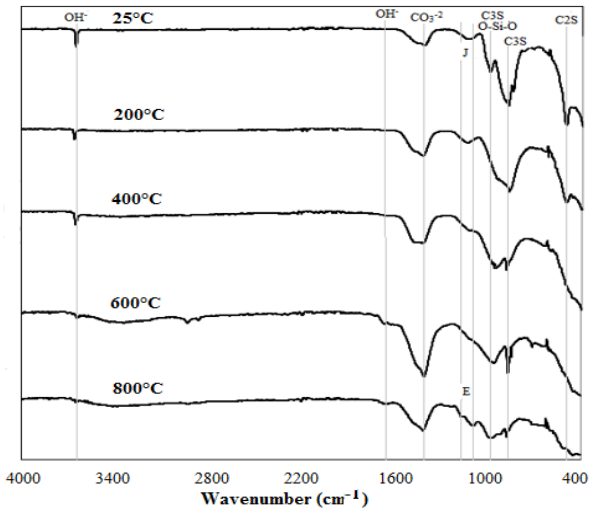

Figure 4. FTIR analysis of heated cement paste at different temperatures.

The absorption bands at 850–800 cm^{-1} and 450–400 cm^{-1} correspond to alite (C3S) and belite (C2S) phases, respectively. The band near 520 cm^{-1} is attributed to the O–Si–O bending vibration in the C–S–H gel, indicating its formation and subsequent reduction with increasing temperature. As the exposure temperature rises, noticeable changes occur in the intensity and sharpness at the peaks. The characteristic bands related to CO_3^{-2}, –OH (from both water and portlandite), C–S–H, O–Si–O, ettringite, and gypsum (SO_4^{-2}) gradually weaken or disappear, reflecting the progressive dehydration and decomposition of hydrated products. Conversely, the peak intensities associated with C2S and C3S increase steadily, suggesting the recrystallization or reformation of these clinker phases at elevated temperatures. Table 2 summarizes the relative intensities of the main absorption bands identified in the spectra (Tantawy 2017; Matossi 1949; Gadsden 1975; Bakharev 2005; Alonso et al. 2013).

Table 2. Characteristic infrared bands of components.

	C2S	*C3S*	*C-S-H*	*Etrin.*	*Jibs*	*Cals*	*H_2O*	*Port.*
Band cm^{-1}	450	937	975	1115	1144	1432	3455	3642

BET and BJH Analysis

The specific surface area (S_{BET}) of cement paste samples, total pore volume, and micro pore volume are reported in Table 3, while Figure 5 shows their pore size distribution curves obtained using the BJH method, which is particularly suitable for meso pores with diameters between 2 and 50 nm.

Table 3. Surface properties of cement pastes.

Temp. (°C)	*S_{BET} (m^2/g)*	*Total Pore Volume (cm^3/g)*	*Micropore Volume (cm^3/g)*
25	21.93	0.038	0.010
200	13.03	0.068	0.0065
400	13.70	0.088	0.0070
600	13.89	0.094	0.0068
800	8.23	0.035	0.0039

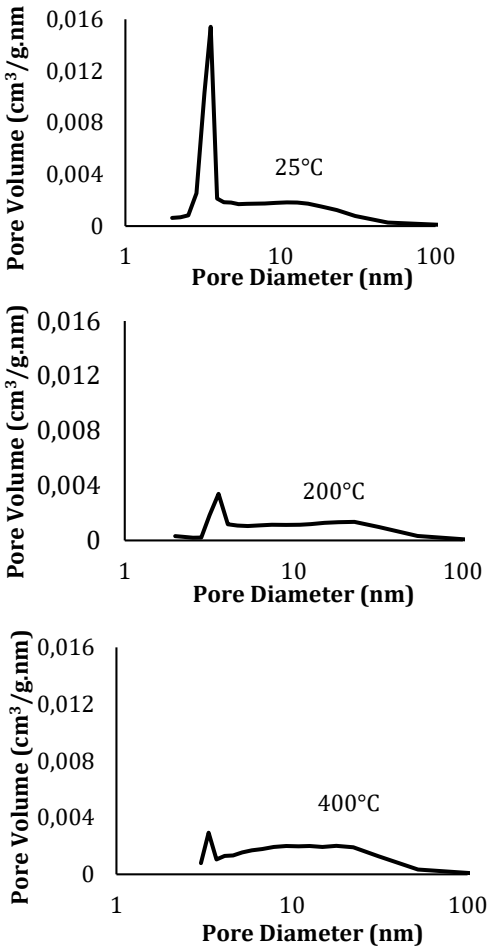

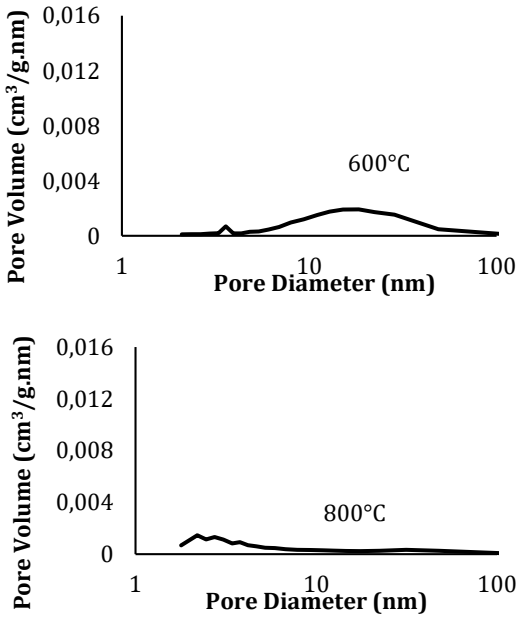

Figure 5. Pore characterization of cement pastes at different temperature.

The total pore volume of the cement paste increases progressively with temperature up to a certain point, indicating the development of additional pores due to thermal decomposition and dehydration. As the temperature rises, the microstructure gradually transforms into a more open and porous macrostructure. Conversely, the specific surface area (S_{BET}) decreases with increasing temperature, reflecting the collapse of fine gel pores and the coalescence of smaller pores into larger ones.

At 25°C, the cement paste exhibits a total pore volume of 0.038 cm^3/g, which increases to 0.094 cm^3/g at 600°C. Beyond this temperature, particularly after 800°C, severe structural damage and coarsening of pores are evident. The observed increase in total pore volume with rising temperature is mainly due to the expansion of macro pores. The initial rise up to 200°C results from the loss of physically bound and chemically bound water, as well as partial decomposition of C–S–H gel. At around 400°C, the further increase in macro pore volume is associated with the decomposition of CH (portlandite). The maximum total pore volume is reached near 600°C, corresponding to the degradation of calcite ($CaCO_3$) and the complete disintegration of the cement matrix (Zhang&Ye 2011). In the literature, it was determined the BET surface area of OPC hydrated for 28 days at 77 K with N_2 as 8.3 m^2/g (Odler 2003). In one study, the surface area of cement paste was measured using different techniques and different adsorbents by applying different drying methods. Accordingly, the BET surface area measurement with N_2 gas was measured as 79.4 m^2/g (Thomas et al. 1999).

The BET surface area of the cement paste in the present study was calculated as 21.93 m^2/g. In comparison, values reported in the literature vary significantly. These discrepancies can be attributed to differences in cement type, sample preparation, degree of grinding, hydration age, and BET measurement parameters such as degassing temperature and duration. Additionally, the extent of hydration and pore structure development in the samples can influence the accessible surface area, which may explain why the measured surface area in the current study falls between the literature values.

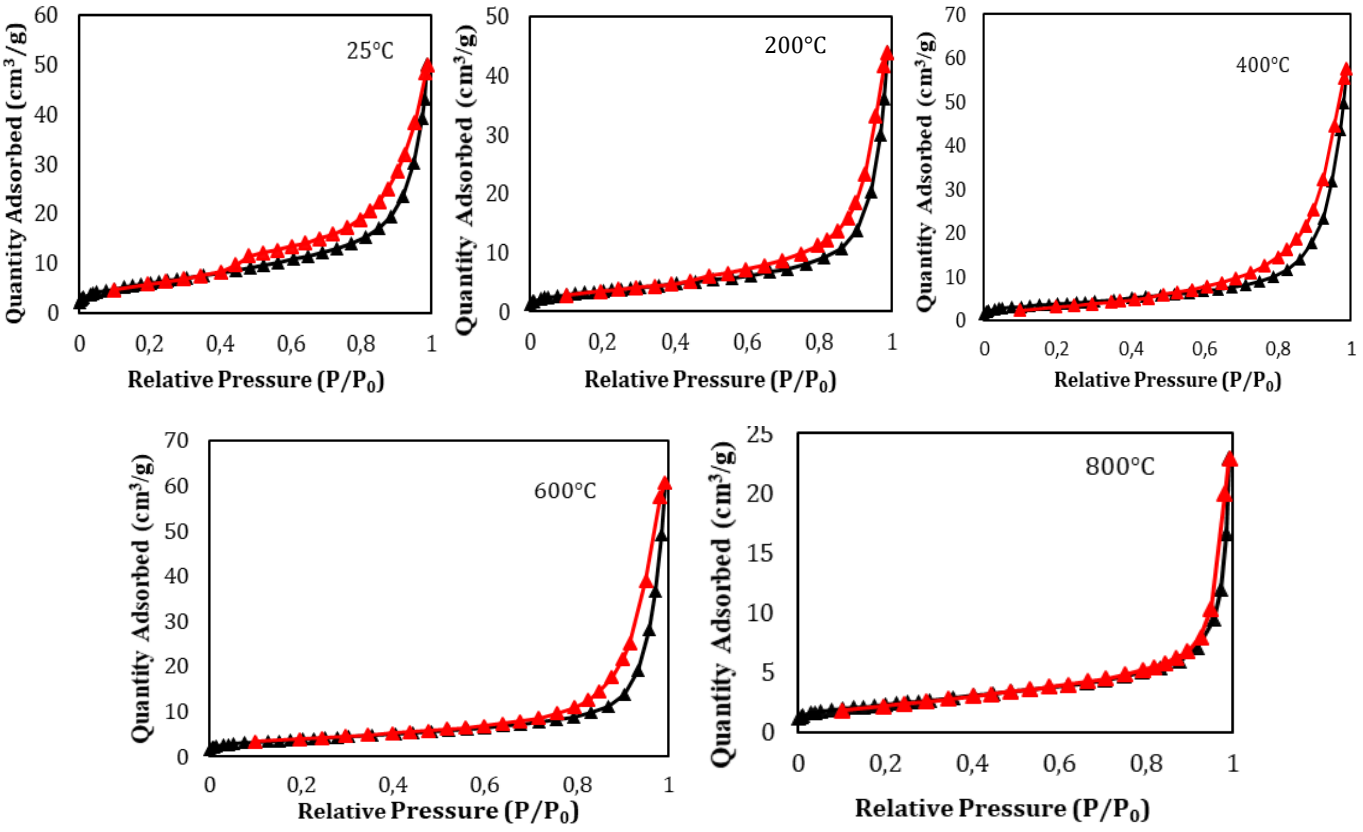

Figure 6. The nitrogen adsorption– desorption isotherms of cement pastes at different temperatures

As can be seen from Figure 6, the nitrogen adsorption–desorption isotherms and related pore parameters reveal the progressive structural evolution of the cement paste with increasing temperature. At 25°C, the isotherm exhibits the

typical properties of hydrated cement paste, dominated by high micro porosity originating from the C–S–H gel, consistent with the highest BET surface area and micropore volume. Upon heating to 200°C, dehydration of physically bound water leads to a decrease in micropore volume and BET surface area, while total pore volume increases due to enlargement of capillary pores. At 400°C, the onset of portlandite decomposition and structural reorganization causes further growth of meso- and macro pores, producing a steeper capillary condensation zone in the isotherm and the highest total pore volumes. This trend continues at 600°C. However, exposure to 800°C causes partial recrystallization, leading to significant losses in both surface area and pore volume; As a result, a significant decrease in adsorption is observed in the isotherm. The results show a transition from a microporous structure at low temperatures to an expanded capillary pore network at intermediate temperatures, followed by densification and pore collapse at the highest temperature.

TG-DTG/DSC Analysis

The microstructural evaluations reveal that the characteristics of the cement paste changed systematically with increasing temperature. These modifications can be attributed to several thermal effects, including:

- Removal of water from pores,
- Degradation of hydration products,
- Chemical phase transformations,
- Destruction and deformation of the microstructure, and
- Conversion of the microstructure into a macro porous structure.

Thermal analyses were conducted to determine the chemical phenomena responsible for these transformations. Figure 7 presents the TG curves of the cement paste obtained at heating rates of 2.5, 5, and 10°C/min within the temperature range of 25–1000°C. Figures 8 and Figure 9 illustrate the corresponding DTG and DSC curves. In the DSC plots, the characteristic thermal parameters, namely onset temperature (To), peak maximum (Tp), and completion temperature (Tc), are clearly identified.

The TG–DTG/DSC curves demonstrate that dehydration, dehydroxylation, and decarbonation reactions occur sequentially with increasing temperature. Moreover, these reactions shift toward higher temperatures as the heating rate increases, indicating a kinetic delay in thermal decomposition processes due to heat transfer limitations (Li et al, 2005).

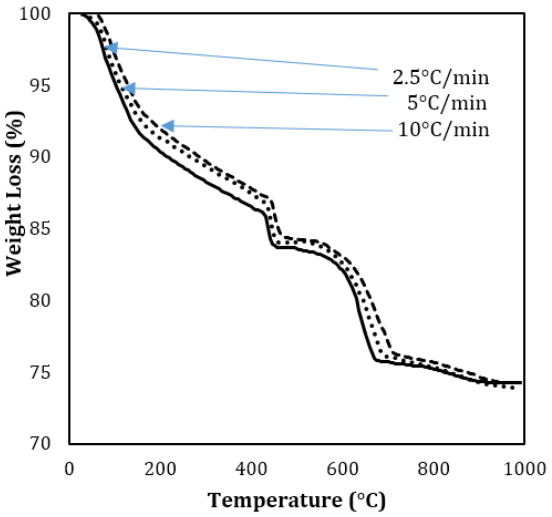

Figure 7. TG profiles of cement paste.

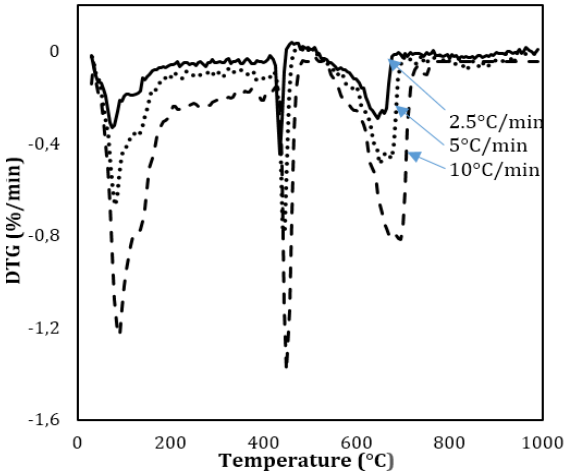

Figure 8. DTG profiles of cement paste.

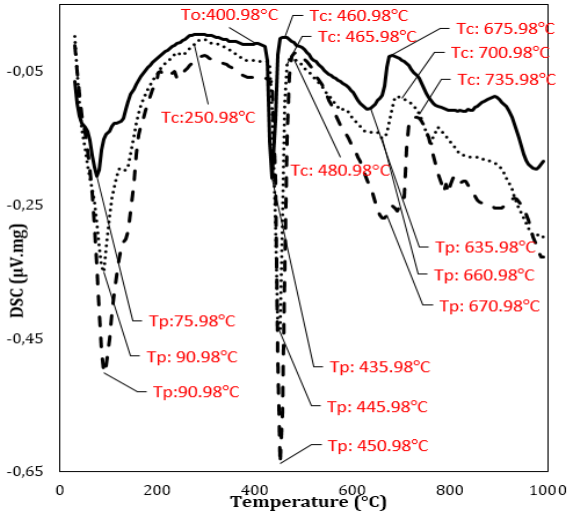

Figure 9. DSC profiles of cement paste.

The total weight loss of the cement paste is approximately 24% for all heating rates. Three dominant endothermic processes, accompanied by corresponding weight losses up to 1000°C, can be clearly distinguished in the TG–DTG/DSC curves. Accordingly, the curves were divided into three distinct regions:

Region I (Dehydration, 25–250°C):
This region represents a weight loss of 10–13%, primarily attributed to the dehydration of various hydrates—particularly C–S–H and ettringite—as well as the release of physically adsorbed water from interlayer and capillary pores (Alarcon-Ruiz et al. 2005). At this stage, the C–S–H structures begin to lose chemically bound water. The dehydration process is characterized by a sharp peak in the DTG curve and a corresponding endothermic peak in the DSC profile.

The chemical reaction for the dehydration process is given below (Zhang & Ye, 2012):

$$(CaO)_aSiO_2(H_2O) \leftrightarrow \underbrace{(CaO)_aSiO_2(H_2O)_{b-c}}_{\text{C-S-H}} + H_2O(g) \qquad (1)$$

Region II (Dehydroxylation 400-500°C):
The weight loss associated with the dehydroxylation of portlandite (CH) is approximately 3%.

$$Ca(OH)_2 \rightarrow CaO + H_2O \qquad (2)$$

In the DTG curve, it can be observed that the onset temperatures of the dehydroxylation reactions remain nearly constant, whereas the peak and completion temperatures move toward higher values as the heating rate increases. According to the literature, the onset temperature of the CH dehydroxylation reaction is a critical parameter and is widely used as an indicator for assessing the thermal history of cementitious materials (Alorcon-Ruiz et al., 2005).

In a previous study on 28-day-hydrated cement paste, TG–DTG and DSC analyses revealed a three-stage degradation profile, in which the decomposition of portlandite (CH) at approximately 400°C was highlighted as a key thermal event (Kontori et al., 2009). The mass-loss fraction associated with this CH dehydroxylation region is commonly used as an indicator of pozzolanic activity, since pozzolanic additives consume CH and consequently reduce the magnitude of this degradation peak. Therefore, the percentage of mass loss determined from the TG curve in this temperature interval provides valuable insight into the pozzolanic contribution of supplementary materials incorporated into cement paste.

Region III (Decarbonation, 500–750°C):
In this region, a weight loss of approximately 8% occurs, corresponding to the decarbonation of $CaCO_3$.

$$CaCO_3 \rightarrow CaO + CO_2 \quad (3)$$

XRD results confirm the presence of calcite in the samples prior to decomposition. A considerable amount of calcite is typically present in OPC-based systems, as it is often added as a filler material (European Comittee, 2000). The DSC curve indicates that the degradation of calcite is an endothermic process, consistent with the literature.
The TG–DTG/ DSC measurements were conducted under various heating rates to examine the effect on the decomposition temperatures in all three identified regions. It has been observed that increasing the heating rate causes a gradual increase in decomposition temperatures. This behavior is linked to the kinetic limitations imposed by accelerated heating. This observation highlights the importance of considering heating rate effects when evaluating the thermal stability and reaction mechanisms of sample under high temperatures.

Kinetics analysis

The degradation reactions of cement paste at elevated temperatures are highly complex; therefore, the kinetic analysis should be performed by dividing the process into distinct temperature regions (Zhang&Ye, 2012). The analysis begins with calculating the conversion degree (α) from the TG–DTG curves for each heating rate. Establishing the relationship between temperature and conversion is essential for kinetic interpretation. Through this approach, kinetic analysis enables the elucidation of the reaction mechanisms (g(α)) governing the multi-step degradation behavior of cement paste under elevated temperature.

The function g(α) represents the integral kinetic model that defines the mechanism controlling the reaction. In this study, several solid-state reaction models (listed in Tables 4–6) were used to evaluate possible mechanisms. The selection of an appropriate g(α) function is a critical step in kinetic analysis, as it directly influences the determination of kinetic parameters. Furthermore, the activation energy (Ea) plays an indispensable role: the higher the activation energy, the more difficult the reaction process becomes. For the dehydration reactions of cement paste, the model-fitting approach was employed to determine the most suitable reaction mechanism, while the Ortega method was applied to predict the kinetic characteristics defined by Ea, A: pre-exponential factor (Ortega, 1996).. According to the Ortega method, these parameters are obtained using Equation (1):

$$\ln(g(\alpha)) = \ln(\frac{AEa}{\beta R}) - 5.331 - 1.052(\frac{Ea}{RT}) \quad (1)$$

In kinetic evaluation, a linear relationship is expected when plotting lng(α) versus 1000/T, and the slope corresponds to –1.052 Ea/R. g(α) represents the reaction mechanism governing the overall process. When g(α) is correctly determined, the graph of ln g(α) versus 1/T shows a strong linear correlation (R^2) in regression analysis. For the defined g(α) function, the activation energy (Ea) is derived from the slope of the fitted line, while the pre-exponential factor (ln A) is obtained by entering the Ea value for each conversion degree (α) into Equation 1.

The kinetic parameters calculated for different temperature ranges are summarised in Tables 4, 5, and 6. For each range, the activation energy and dominant mechanism controlling the dehydration of cement paste at various heating rates have been determined.

Region I: The dehydration process is controlled by a second-order chemical reaction,
F_2:$(1-\alpha)^{-1}$-1, with an activation energy of 42.92 kJ/mol.
Region II: The reaction is governed by a random nucleation and subsequent growth mechanism, A_3:$[-\ln(1-\alpha)]^{2/3}$, with an activation energy of 141.79 kJ/mol and a pre-exponential factor lnA=21.4.
For comparison, the literature reports an activation energy of 151.82 kJ/mol and ln A between 20–25 for CH dehydroxylation using the isoconversional Friedman method, indicating that the present results are consistent with previous studies (Zhang & Ye, 2012).
Region III: corresponding to the decarbonation of $CaCO_3$, the reaction is governed by an interphase-limited surface reaction, R_2: $1-(1-\alpha)^{1/2}$, with an activation energy of approximately 152.11 kJ/mol and lnA=16.15. The calculated activation energies and pre-exponential factors for all three regions show good agreement with literature values, confirming the reliability of the kinetic analysis and the proposed reaction mechanisms.

In the study by Zhang & Ye (2012), the dehydration kinetics of cement paste were evaluated using TG analysis, and the activation energies were determined via the Friedman isoconversional method. Their results indicated that the activation energy associated with the first degradation region was from 83.69 to 371.93 kJ/mol, while the activation energy corresponding to CH dehydroxylation was reported as 151.82 kJ/mol. In comparison, the activation energy calculated for Region I in our study, representing the degradation of C–S–H was 42.92 kJ/mol, and the activation energy for CH degradation (Region II) was determined as 141.79 kJ/mol. Despite methodological differences, the activation energy values obtained in both studies demonstrate good consistency, confirming similar thermal decomposition behavior of cement paste.

Table 4. (I. Region) Activation energies calculated from different models.

Mechanisms		*g(α)*	*β= 2.5*	*β= 5*	*β= 10*
Chemical reaction (first-order)	F_1	-ln (1-α)	29,14	27,04	29.67
Chemical reaction (second-order)	**F_2**	**$(1-\alpha)^{-1}-1$**	**41,66**	**41,68**	**45.39**
Chemical reaction (third-order)	F_3	$[(1-\alpha)^{-2}-1]/2$	57,31	60,50	66.39
One-dimensional diffusion	D_1	α^2	32,85	43,03	47.18
Two-dimensional diffusion	D_2	$\alpha+(1-\alpha)\ln(1-\alpha)$	30,42	39,89	43.60
Ginstling-Brounshtein equation	D_4	$(1-2\alpha/3)-(1-\alpha)^{2/3}$	47,51	50,16	46.07
Contracted geometry shape (cylindrical)	R_2	$1-(1-\alpha)^{1/2}$	24,30	25,65	28.14
Contracted geometry shape (sphere)	R_3	$1-(1-\alpha)^{1/3}$	25,82	27,25	29.89
Nucleation and growth (n=2)	A_2	$-\ln(1-\alpha)^{1/2}$	14,57	15,37	16.88
Nucleation and growth (n=3)	A_3	$-\ln(1-\alpha)^{1/3}$	9,71	10,25	11.25
Mample power law (n=2)	P_2	$\alpha^{1/2}$	10,19	10,76	11.79
Mample power law (n=3)	P_3	$\alpha^{1/3}$	6,80	7,18	7.86
Mample power law (n=4)	P_4	$\alpha^{1/4}$	5,09	5,39	5.89

Table 5. (II. Region) Activation energies calculated from different models.

Mechanisms		*g(α)*	*β= 2.5*	*β= 5*	*β= 10*
Chemical reaction (first-order)	F_1	-ln (1-α)	424,90	447,98	380,36
Chemical reaction (second-order)	F_2	$(1-\alpha)^{-1}-1$	589,30	715,45	610,70
Chemical reaction (third-order)	F_3	$[(1-\alpha)^{-2}-1]/2$	793,35	830,07	717,13
One-dimensional diffusion	D_1	α^2	615,55	653,91	548,35
Two-dimensional diffusion	D_2	$\alpha+(1-\alpha)\ln(1-\alpha)$	679,61	719,99	606,16
Ginstling-Brounshtein equation	D_4	$(1-2\alpha/3)-(1-\alpha)^{2/3}$	706,45	747,74	630.51
Contracted geometry shape (cylindrical)	R_2	$1-(1-\alpha)^{1/2}$	360,58	381,45	321.92
Contracted geometry shape (sphere)	R_3	$1-(1-\alpha)^{1/3}$	380,69	402,24	340.16
Nucleation and growth (n=2)	A_2	$-\ln(1-\alpha)^{1/2}$	212,44	223,99	190.18
Nucleation and growth (n=3)	**A_3**	**$-\ln(1-\alpha)^{1/3}$**	**141,63**	**149,32**	**134.43**
Mample power law (n=2)	P_2	$\alpha^{1/2}$	153,88	163,47	137.09
Mample power law (n=3)	P_3	$\alpha^{1/3}$	102,59	108,98	91.39
Mample power law (n=4)	P_4	$\alpha^{1/4}$	76,95	81,74	68.54

Table 6. (III. Region) Activation energies calculated from different models.

Mechanisms		*g(α)*	*β= 2.5*	*β= 5*	*β= 10*
Chemical reaction (first-order)	F_1	-ln (1-α)	180,86	185,63	168,35
Chemical reaction (second-order)	F_2	$(1-\alpha)^{-1}-1$	248,08	254,95	230,96
Chemical reaction (third-order)	F_3	$[(1-\alpha)^{-2}-1]/2$	331,15	340,62	308,32
One-dimensional diffusion	D_1	α^2	264,82	271,43	246,46
Two-dimensional diffusion	D_2	$\alpha+(1-\alpha)\ln(1-\alpha)$	291,57	298,96	271,34
Ginstling-Brounshtein equation	D_4	$(1-2\alpha/3)-(1-\alpha)^{2/3}$	302,64	310,40	281,69
Contracted geometry shape (cylindrical)	**R_2**	**$1-(1-\alpha)^{1/2}$**	**154,34**	**158,32**	**143,66**
Contracted geometry shape (sphere)	R_3	$1-(1-\alpha)^{1/3}$	162,65	166,88	151,40
Nucleation and growth (n=2)	A_2	$-\ln(1-\alpha)^{1/2}$	90,43	92,81	84,18
Nucleation and growth (n=3)	A_3	$-\ln(1-\alpha)^{1/3}$	60,28	61,87	56,12
Mample power law (n=2)	P_2	$\alpha^{1/2}$	66,21	61,61	61,61
Mample power law (n=3)	P_3	$\alpha^{1/3}$	44,14	41,07	41,07
Mample power law (n=4)	P_4	$\alpha^{1/4}$	33,13	30,80	30,80

CONCLUSIONS

This study provides an innovative and quantitative assessment of the high-temperature degradation mechanisms of CEM I cement paste by combining mechanical (Compressive Strength), microstructural (SEM-EDS), physicochemical (XRD, FT-IR), textural (BET), thermal (TG–DTG/DSC), and kinetic analyses. Unlike previous studies that focus mainly on isolated degradation phenomena or mechanical strength changes, this work offers an understanding of the coupled chemical, microstructural, and textural transformations occurring between 25°C and 1000°C. The novelty of this research is its quantitative integration of activation-energy-based thermal decomposition kinetics analysis with microstructural collapse and porosity evolution, establishing a unified and predictive degradation model for CEM I cement paste under high-temperature conditions.

The Compressive Strength results revealed a progressive decline with increasing temperature: 33.5% reduction was observed up to 400°C, while values could not be recorded at 600°C and 800°C due to structural collapse. This highlights the critical vulnerability of hydrated phases, particularly C–S–H and ettringite, to thermal exposure.

The XRD analyses confirmed the phase transformations, showing the loss of portlandite (CH) and partial decomposition of C–S–H into C2S and C3S, as well as decarbonation of calcite at 500–750°C.

The FT-IR spectra further corroborated these changes, indicating the disappearance of OH stretching bands from CH and H_2O, along with the weakening of carbonate-related peaks, reflecting both dehydroxylation and decarbonation processes.

The SEM-EDS images demonstrated progressive microstructural degradation: deformation and partial collapse of CH crystals and C–S–H gel were observed with increasing temperature. EDS analysis indicated the reduction of Ca

content due to CH dehydroxylation and partial decalcification of C–S–H gel, consistent with the other findings.

The BET measurements quantified the textural changes, showing a decrease in specific surface area (from 21.93 m^2/g at 25°C to lower values at 400°C) and an increase in total pore volume, reflecting coarsening of the pore structure. At 800°C, total pore volume slightly decreased due to the collapse of hydrated phases, indicating a transition to a more compact, yet highly degraded, matrix.

TG–DTG/DSC analyses identified three main thermal events:
(i) dehydration of C–S–H, ettringite, and free water (25–200°C) with a mass loss of 10–13%,
(ii) dehydroxylation of CH (400–500°C) with ~3% mass loss, and
(iii) decarbonation of calcite (500–750°C) with ~8% mass loss. These thermal events closely correlate with observed structural and chemical changes from XRD, FT-IR, and SEM-EDS.

Kinetic analysis using the Ortega method revealed the activation energies of thermal decomposition: 42.92 kJ/mol for dehydration (C-S-H) process, 141.79 kJ/mol for dehydroxylation (CH), and 152.11 kJ/mol for decarbonation of calcite emphasize the differential thermal stability of hydration products and carbonates. This quantitative linking of activation energies with microstructural collapse and porosity evolution represents the primary novelty of the study, providing a unified model for high-temperature degradation of CEM I cement paste.

Future research could explore;
(i)incorporation of fibers or additives to mitigate dehydration-induced cracking,
(ii) reinforcement strategies to reduce pore coarsening, and
(iii)predictive numerical models using the kinetic parameters obtained here.

Overall, this study quantitatively demonstrates that elevated temperatures cause significant degradation of hydration products, microstructural collapse, porosity changes, and drastic reduction in compressive strength. The integrated methodology and quantified results provide critical insights for predicting fire-induced damage, guiding repair strategies, and designing more fire-resistant cementitious composites.

ACKNOWLEDGEMENTS

The financial support of this study was provided by the Atatürk University BAP project (Project No: FHD-2018-6654).

REFERENCES

Abdelmelek, N., Lubloy, E. (2021). Evaluation of the mechanical properties of high strength cement paste at elevated temperatures using metakaolin. *Journal of Thermal Analysis and Calorimetry, 145*, 2891–2905. https://doi.org/10.1007/s10973-020-09992-2

Alarcon-Ruiz, L., Platret, G., Massieu, E., Ehrlacher, A. (2005). The use of thermal analysis in assessing the effect of temperature on a cement paste. *Cement and Concrete Research, 35*(3), 609–613. https://doi.org/10.1016/j.cemconres.2004.06.015

Alanso, M.M., Palacios, M., Puertas, F. (2013). Effect of polycarboxylate-ether admixtures on calcium aluminate cement pastes, Part 2: Hydration studies. *Industrial & Engineering Chemistry Research, 52*, 17330-17340. https://doi.org/10.1021/ie401616f

Arıöz, Ö. (2007). Effects of elevated temperatures on properties of concrete. *Fire Safety Journal, 42*(8), 516–522. https://doi.org/10.1016/j.firesaf.2007.01.003

Bakharev, T. (2005). Geopolymeric materials prepared using class F fly ash and elevated temperature curing. *Cement and Concrete Research, 35*(6), 1224. https://doi.org/10.1016/j.cemconres.2004.06.031

Bingöl, A.F., Gül, R. (2004). Compressive strength of lightweight aggregate concrete exposed to high temperatures. *Indian Journal of Engineering and Materials Sciences, 11*, 68–72.

Bingöl, A.F., Gül, R. (2009). Effect of elevated temperatures and cooling regimes on normal strength concrete. *Fire and Materials, 33*, 79–88. https://doi.org/10.1002/fam.987

Boquera, L., Castro, J.R., Pisello, A.L., Fabiani, C., D'Alessandro, A., Ubertini, F., Cabeza, L.F. (2021). Thermal and mechanical performance of cement paste under high temperature thermal cycles. *Solar Energy Materials and Solar Cells, 231*, 111333. https://doi.org/10.1016/j.solmat.2021.111333

European Committee for Standardization. (2000). *Cement: Common cements* (PrEN 197-1, CEN/TC51/WG 6 rev., Final Draft).

Gadsden, J.A. (1975). *Infrared spectra of minerals and related inorganic compounds* (3rd ed.). Butterworths.

Handoo, S.K., Agarwal, S., Agarwal, S.K. (2002). Physicochemical, mineralogical, and morphological characteristics of concrete exposed to elevated temperatures. *Cement and Concrete Research, 32*, 1009–1018. https://doi.org/10.1016/S0008-8846(01)00736-0

Hüsem, M. (2006). The effects of high temperature on compressive and flexural strengths of ordinary and high-performance concrete. *Fire Safety Journal, 41*, 155–163. https://doi.org/10.1016/j.firesaf.2005.12.002

Kasaniya, M., Thomas, M.D.A., Moffatt, T., Hossack, A. (2024). Microstructure and microanalysis of Portland cement pastes with high w/c ratios. *Cement and Concrete Research, 183*, 107575. https://doi.org/10.1016/j.cemconres.2024.107575

Khoury, G.A. (1992). Compressive strength of concrete at high temperatures: Reassessment. *Magazine of Concrete Research, 44*, 291–309. https://doi.org/10.1680/macr.1992.44.161.291

Kontori, E., Perraki, T., Tsivilis, S., Kakali, G. (2009). Zeolite blended cements: Evaluation of their hydration rate by means of thermal analysis. *Journal of Thermal Analysis and Calorimetry, 96*, 993–998. http://doi.org/10.1007/s10973-009-0056-x

Li, S., Whitely, N., Xu, W., Pan, W.P. (2005). Characterization of Coal by Thermal Analysis Methods, Thermal Analysis

Laboratory, Materials Characterization Centre, Western Kentucky University.

Li, Y., Luo, Y., Du, H., Liu, W., Tang, L., Xing, F. (2022). Evolution of microstructural characteristics of carbonated cement pastes subjected to high temperatures evaluated by MIP and SEM. *Materials, 15*, 6037. https://doi.org/10.3390/ma15176037

Matossi, F. (1949). Vibration frequencies and binding forces in some silicate groups. *Journal of Chemical Physics, 17*, 679. https://doi.org/10.1063/1.1747369

Odler, I. (2003). The BET-specific surface area of hydrated Portland cement and related materials. *Cement and Concrete Research, 33*, 2049–2056. https://doi.org/10.1016/S0008-8846(03)00225-4

Ortega, A. (1996). Some successes and failures of the methods based on several experiments. *Thermochimica Acta, 284*, 379–387. https://doi.org/10.1016/0040-6031(95)02766-1

Peng, G.F., Huang, Z.S. (2008). Change in microstructure of hardened cement paste subjected to elevated temperatures. *Construction and Building Materials, 22*, 593. https://doi.org/10.1016/j.conbuildmat.2006.11.002

Poon, C.S., Azhar, S., Anson, M., Wong, Y.L. (2001). Comparison of the strength and durability performance of normal and high-strength pozzolanic concretes at elevated temperatures. *Cement and Concrete Research, 31*(9), 1291–1300. https://doi.org/10.1016/S0008-8846(01)00580-4

Poon, C.S., Azhar, S., Anson, M., Wong, Y.L. (2003). Performance of metakaolin concrete at elevated temperatures. *Cement and Concrete Composites, 25*(1), 83–89. https://doi.org/10.1016/S0958-9465(01)00061-0

Poon, C.S., Shui, Z. H., Lam, L. (2004). Compressive behavior of fiber reinforced high-performance concrete subjected to elevated temperatures. *Cement and Concrete Research, 34*, 2215–2222. https://doi.org/10.1016/j.cemconres.2004.02.011

Tantawy, M.A. (2017). Effect of high temperatures on the microstructure of cement paste. *Journal of Materials Science and Chemical Engineering, 5*, 33–48. http://doi.org/10.4236/msce.2017.511004

Thomas, J.J., Jennings, H.M., Allen, A.J. (1999). The surface area of hardened cement paste as measured by various techniques. *Concrete Science and Engineering, 1*, 45–64. https://doi.org/10.1016/S0008-8846(98)00049-0

TS EN 12390-3. (2010). Beton-Sertleşmiş beton deneyleri-Bölüm 3: Deney numunelerinin basınç dayanımının tayini, Türk Standartları Enstitüsü, Ankara, Türkiye.

Zhang, Q., Ye, G. (2011). Microstructure analysis of heated Portland cement paste. *Procedia Engineering, 14*, 830–836. https://doi.org/10.1016/j.proeng.2011.07.105

Zhang, Q., Ye, G. (2012). Dehydration kinetics of Portland cement paste at high temperature. *Journal of Thermal Analysis and Calorimetry, 110*, 153–158. http://doi.org/10.1007/s10973-012-2303-9